

Cite this: *Chem. Sci.*, 2023, 14, 7512

All publication charges for this article have been paid for by the Royal Society of Chemistry



Received 7th February 2023

Accepted 28th May 2023

DOI: 10.1039/d3sc00677h

rsc.li/chemical-science

# Shape tunability of copper nanocrystals deposited on nanorods†

Yuexing Chen  and Lilac Amirav \*

The significant role of metal particle geometry in dictating catalytic activity, selectivity, and stability is well established in heterocatalysis. However, this topic is rarely explored in semiconductor–metal hybrid photocatalytic systems, primarily due to the lack of synthetic control over this feature. Herein, we present a new synthetic route for the deposition of metallic Cu nanoparticles with spherical, elliptic, or cubic geometrical shapes, which are selectively grown on one side of the well-established CdSe@CdS nanorod photocatalytic system. An additional multipod morphology in which several nanorod branches are combined on a single Cu domain is presented as well. Cu is an earth-abundant low-cost catalyst known to promote a diverse gallery of organic transformations and is an excellent thermal and electrical conductor with interesting plasmonic properties. Its deposition on cadmium chalcogenide nanostructures is enabled here *via* mitigation of the reaction kinetics such that the cation exchange reaction is prevented. The structural diversity of these sophisticated nanoscale hybrid systems lays the foundations for shape–activity correlation studies and employment in various applications.

## 1. Introduction

Photocatalytic solar-to-fuel conversion is globally acknowledged as a compelling renewable energy source that simultaneously mitigates the generation and storage challenges. The design of effective photocatalytic systems at the nanoscale depends on our ability to correlate functionality with composition, structure, and morphology. Platinum-tipped cadmium sulfide rod with an embedded cadmium selenide seed (CdSe@CdS–Pt) offers an exemplary design, demonstrating the considerable benefits of employing hybrid nanostructures.<sup>1</sup> This system attained nearly perfect 100% photon-to-hydrogen production efficiency,<sup>2</sup> and later a complete redox cycle and record-high solar to chemical conversion efficiency.<sup>3</sup> These achievements are attributed to systematical tuning of each component in the colloidal hybrid system. Such tunability allows direct control over the chemical and physical properties<sup>4–6</sup> and enables optimization of functionality alongside endowment for additional applications in catalysis,<sup>7</sup> 3D printing,<sup>8</sup> and electronic devices.<sup>9–11</sup>

The quality of the junction formed between the semiconductor light sensitizer and the metallic catalytic domain mandates the availability of charges for promoting the chemistry. Hence, great efforts were devoted to understanding the influence of the metal morphology in the hybrid system and its

effect on the desired catalytic activity. The deposition location, number of metal domains,<sup>12,13</sup> and size<sup>14–18</sup> were thoroughly examined and demonstrated to be vital for optimizing the material's potential in promoting the reaction of interest. However, thus far, the catalyst shape has received minimal attention, predominantly due to the lack of synthetic control over this feature.<sup>19</sup> The significant role of the metal particle geometry (*e.g.*, cubic, spherical, or tetrahedral) in dictating activity, selectivity, and stability is well established in heterocatalysis.<sup>20–22</sup> Shape–reactivity correlations were established over 60 years ago, with reports on different reactivity at crystal edges and corners.<sup>23</sup> It is reasonable to expect a significant influence of the metal cocatalyst shape on photocatalytic processes, with the added complications inherent to its interface with the semiconductor. Hence, attaining the desired control over the metal domain's geometric shape in a semiconductor–metal hybrid photocatalytic system is of great interest. This level of synthetic sophistication is a prerequisite to advance the intelligent design of next generation photocatalytic systems.

Herein, we lay the first foundations towards shape–activity correlation studies in well-designed nanoscale hybrids photocatalytic systems and present a new synthetic route for the deposition of Cu with tunable size and shape on CdSe@CdS nanorods (SR–Cu). The SR–Cu hetero-nanostructures have four appealing geometrical shapes, which include spherical, elliptic, and cubic metallic Cu tips (SR–s-Cu, SR–e-Cu; and SR–c-Cu, accordingly), and an additional multipod morphology in which several SR branches are combined on a single Cu domain.

Schulich Faculty of Chemistry, Technion – Israel Institute of Technology, Haifa 32000, Israel. E-mail: lilac@technion.ac.il

† Electronic supplementary information (ESI) available: Complimentary figures and table. See DOI: <https://doi.org/10.1039/d3sc00677h>

CdSe@CdS nanorods were previously tipped with various metals such as Au,<sup>24</sup> Pt,<sup>25,26</sup> Pd,<sup>27</sup> Co,<sup>28</sup> Ag<sup>29</sup> and Ni<sup>14,30</sup> as well as bimetal combinations.<sup>31,32</sup> In this work we introduce a novel protocol for Cu tipping. Cu is an earth-abundant lowcost alternative to rare and expensive noble metal catalysts.<sup>33</sup> With the metal's ability to access a wide range of oxidation states (Cu<sup>0</sup>, Cu<sup>I</sup>, Cu<sup>II</sup>, and Cu<sup>III</sup>), copper nanoscale catalysts are exploited for the promotion of a gallery of organic transformations, supporting both one- and two-electron pathways, and enabling green and sustainable reaction conditions. Examples in the literature include click chemistry, cross-coupling, C–H functionalization, A3 coupling, clock reactions, borylation, oxidative coupling, redox reactions,<sup>34</sup> and more.<sup>35</sup> Cu is also an excellent thermal and electrical conductor,<sup>36,37</sup> with interesting plasmonic properties.<sup>38</sup> However, cadmium chalcogenide nanostructures were not previously decorated with metallic Cu domains due to the challenging necessity to overcome cation exchange.<sup>39</sup> Additional challenges relate to the difficulties in reducing Cu(II) and Cu(I) precursors due to the low redox potential of Cu which result in uncontrollable reaction kinetics.<sup>40</sup> Furthermore, attaining the required level of control over the shape and morphology of the metallic Cu domains that are deposited on a substrate in a heterogeneous nucleation differs from the already challenging control over homogenous nucleation of freeform metallic nanoparticles.<sup>41</sup>

This work details the means by which we successfully overcome these challenges. Specifically, cation exchange may be avoided *via* introduction of copper(I) acetate/trioctylphosphine complex, which helps modulating the reaction kinetics. This opens up a pathway for “on-off” control of cation exchange and provides the possibility of synthesizing Cu metal on CdSe@CdS nanorods.

The structural diversity, versatility, and high degree of control over the synthesis of the novel SR–Cu heterostructures make them promising potential candidates for various applications.

## 2. Results and discussion

### 2.1 Size-morphological characterization of synthesis products

To allow direct comparison between the various structures, and proper easement of the synthetic conditions leading to their formation, the different sizes and morphologies of the Cu tips were grown on the same batch of CdSe@CdS seeded nanorods (SR). The nanorods were synthesized following a well-established seeded growth procedure that endows preferential heterogeneous nucleation and anisotropic growth of wurtzite (WZ) CdS shell onto the original CdSe seeds.<sup>29,42</sup> A CdSe seed of 2.3 nm diameter was used, and the resulting nanorods were found to have an average diameter of 5 nm and length of about 40 nm (Fig. S1†). In a second step, the purified SR (with fixed concentration) are utilized as substrates for the selective deposition of the metallic Cu component.

SR with elliptic Cu tip shape (SR–e-Cu, Fig. 1a) were prepared by decomposition of a precursor comprised of a complex of copper(I) acetate with TOP, which is used to avoid cation

exchange as described above. Employment of phosphine ligands to modulate the reaction kinetics and enable reduction of the metal precursor rather than cation penetration into the rod's lattice and replacement of Cd atoms was recently demonstrated successfully for the case of Ag tipping of CdSe@CdS nanorods and was adopted here as well.<sup>29</sup> After the reducing agent (TBAB) injection, elliptic Cu domains with dimensions of about 4 × 9 nm were found to selectively grow on one end of SR. As seen in the TEM image in Fig. 1a, the SR–e-Cu exhibits an overall matchstick-like structure, with a distinguished image contrast variation between the rod and metallic domain. Interestingly, an exclusive mono-tip deposition can be observed (*i.e.*, growth of a single Cu tip per rod), in contrast to most of the alternative metal tipping protocols for which some population of rods is always found to have additional tips at the other end of the rods or additionally along its length. Such exclusive mono-tip growth is significant for photocatalytic promotion of multi electron reactions, and solar-to-fuel-conversion.<sup>12</sup> To further confirm the position of Cu on the SR EDS was used to determine the local chemical composition of the SR–e-Cu, and the resulting elemental mapping and corresponding line-scan are presented in Fig. 1b. As expected, the elliptic head shows a brighter contrast in the HAADF image with a strong signal of Cu without a trace of S, while Cd and S are confined to the rod section. The EDS line-scan analyses of an individual SR–e-Cu heterojunction additionally confirms that Cd and S signals are detected across entire stem of the rod, whereas the intensity of Cu signals is higher in the tip region. The results further illustrate that the transverse diameter of the Cu tip is about 5 nm, in good agreement with the TEM measurements. These results verify the exclusive anisotropic deposition of Cu at the tip of SR.

Size and morphology control of the metal domain can be realized by further precise manipulation of the growth kinetics. Heterostructures of SR with spherical Cu tips (SR–s-Cu) were constructed by using a stronger reducing agent, borane-*tert*-butylamine complex (TBAB)/oleylamine (TBAB/OLA). For the formation of spherical Cu tips on SR, the TBAB/oleylamine was injected at 260 °C. The TEM images presented in Fig. 1c exhibit large spherical Cu domains with diameter of ~10–20 nm that are again located at one end of the SR. A lattice spacing of 0.209 nm that corresponds to (111) crystal plane of Cu is clearly seen in the HRTEM in Fig. 1d.

Upon dropping the injection temperature of the reducing agent from 260 °C to room temperature, a cube shape Cu tip was formed, preferentially on one end of the nanorods as shown in Fig. 1e. With a strong image contrast, the faceted tips are clearly identified with a width of around 10 nm. The HRTEM image in Fig. 1f reveals that the growth axis of the WZ SR in all the heterostructures is along the (001) direction. The lattice spacing for the fcc Cu was found to be 0.211 nm, which is assigned to the cubic (111) plane. This analysis is confirmed by its corresponding FFT pattern. Further decrease in the amount of SR that was targeting larger Cu domains resulted with increased homogenous nucleation of free Cu nanoparticles, which were cubic as well (Fig. S2†).



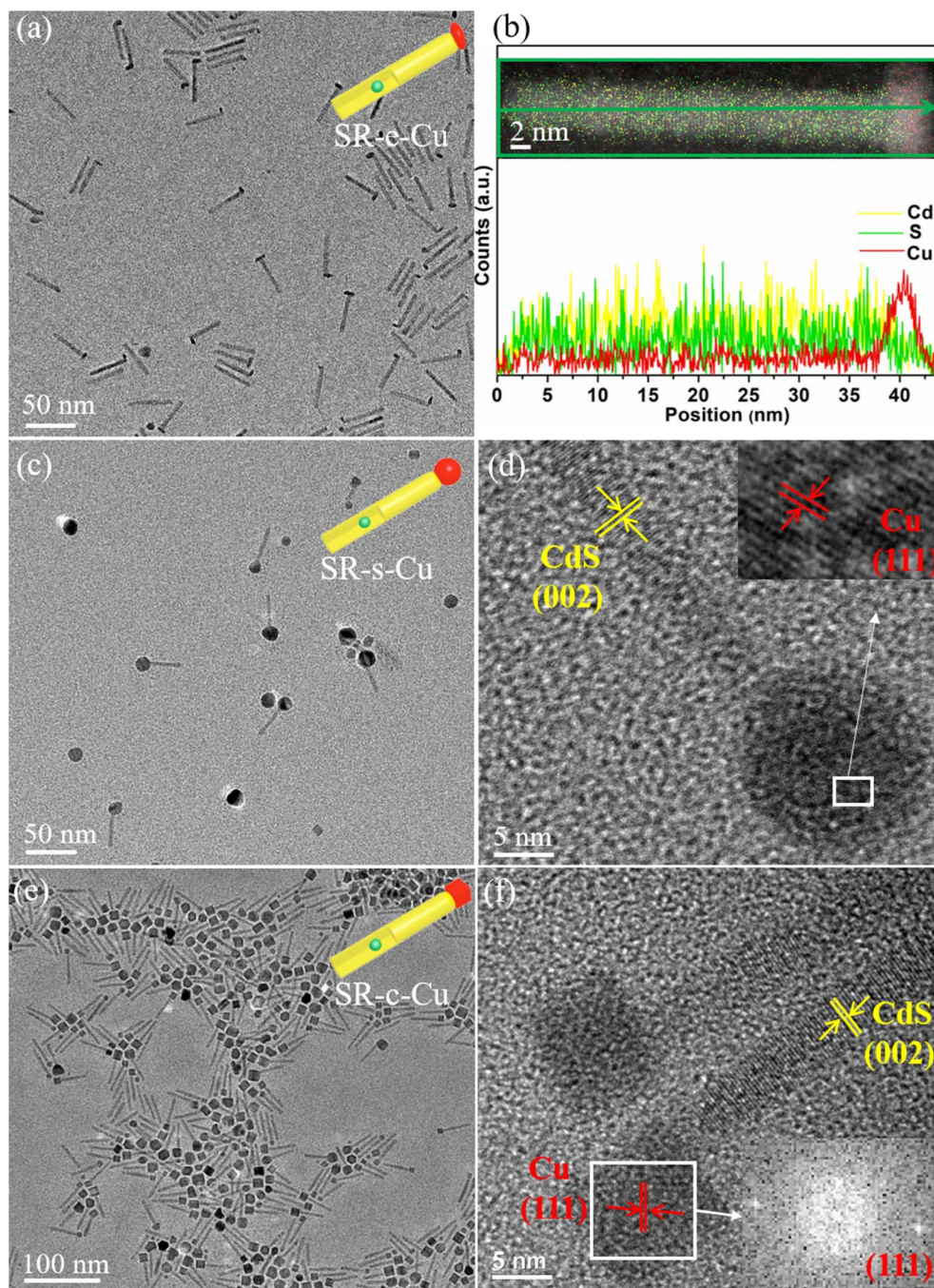


**Fig. 1** (a and b) TEM image and STEM-EDS line-scan analysis of an individual SR-e-Cu heterojunction with EDS mapping shown in the upper inset. SR-e-Cu was synthesized with 0.02 mmol CuOAc-TOP as precursor and TBAB addition at room temperature. (c and d) TEM and HRTEM images of the SR-s-Cu synthesized with 0.04 mmol CuOAc-TOP as precursor and TBAB/OLA injection at 260 °C. (e and f) TEM and HRTEM images of the SR-c-Cu synthesized like SR-s-Cu but 0.02 mmol CuOAc-TOP as precursor. Inset: corresponding FFT pattern in (f).

The concentration ratios of the CuOAc to SR and injection temperature of reducing agents were found to have a considerable effect on the morphologies of SR-Cu heterostructure. When the concentration of the SR was kept the same as that for the synthesis of SR-s-Cu and the concentration of CuOAc was halved, the products were mainly SR-Cu multi-pods, with a branched morphology as illustrated in Fig. 2a (in which Cu is depicted in red). In such multi-pods the Cu domains (slightly

darker part in the center, Fig. 2b and c) act as core from which several SR are branched in a three-dimensional architecture. The relatively large dimensions and mostly the wide size distribution for the Cu core, around 5–50 nm, suggest of potential merging of individual Cu tips. This hypothesis is further supported by the presence of bipods, and tripods in the samples (Fig. 2d). Merging of tips might be accompanied by additional direct growth of the newly formed Cu core. As





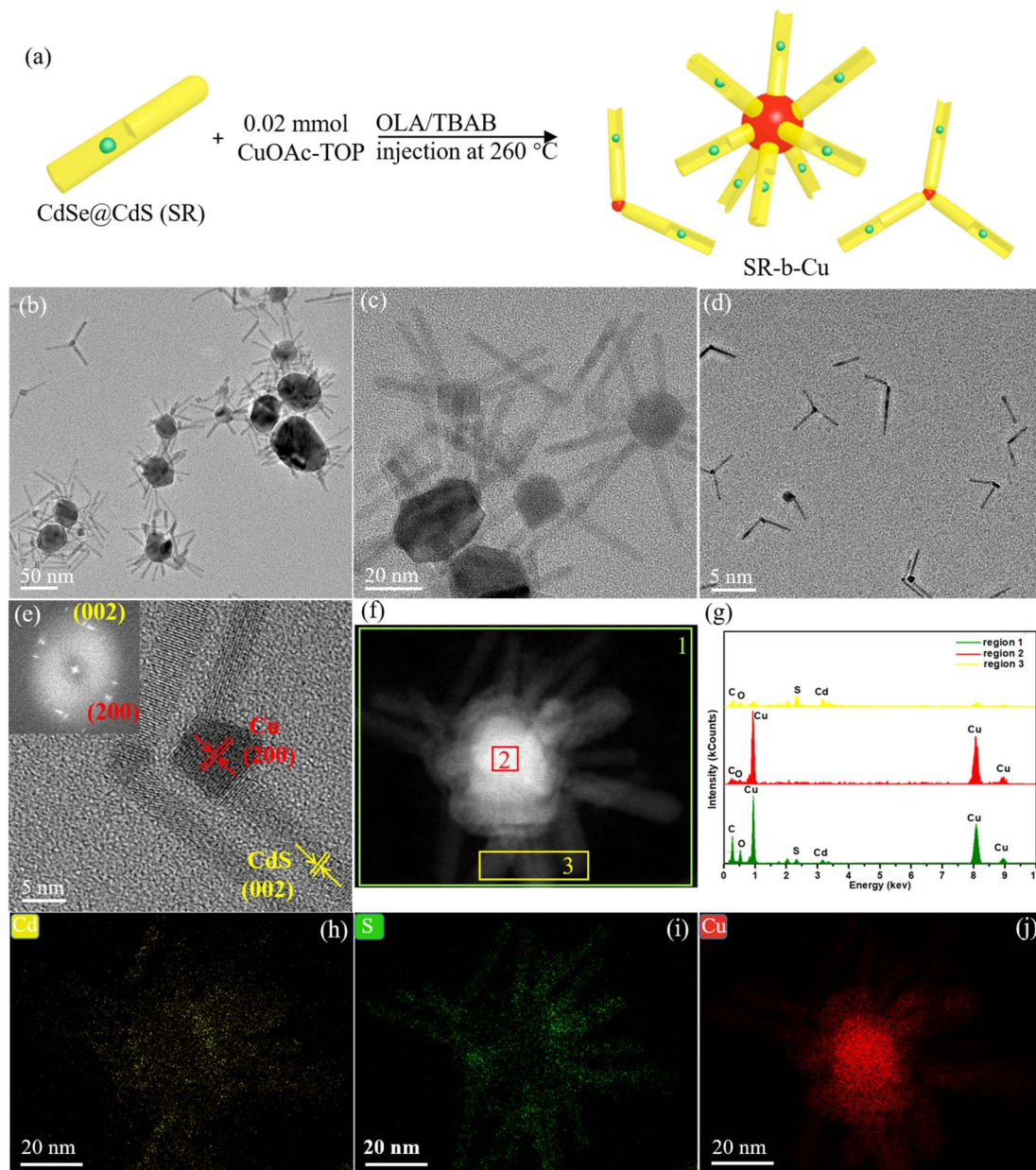


Fig. 2 (a) Illustration of the synthetic path of SR-Cu nanomultipods. (b–d) TEM images of the SR-Cu nanomultipods. (e) HRTEM image of SR-Cu bipods. Inset: corresponding FFT pattern. (f) HAADF image. (g) STEM-EDS spectra recorded from different regions of the single nanomultipod shown in (f). (h–j) Elemental mapping images of this nanomultipod.

revealed in the HR-TEM image of the bipods (Fig. 2e), the lattice fringes of the long arm present an interplanar spacing of 0.336 nm, corresponding to the (002) facet of the WZ CdS, which suggests that the core was growing along the *c*-axis of the arm. The lattice fringes of the Cu core exhibit a clear face-centered-cubic (fcc) packing pattern with the *d*-spacing of 0.182 nm, corresponding to (200) crystal plane of Cu, which is supported by its corresponding FFT pattern. To obtain more information regarding the relative location of Cu and SR, the STEM-EDS spectra (Fig. 2g) are recorded at different positions of single multipods shown in the HAADF image (Fig. 2f). The EDS spectrum of the overall region in Fig. 2f (region 1) shows a strong Cu

signal and relatively weak Cd and S signals. The core part (region 2) exhibits only the Cu signal, while the arms part shows the signals of Cd and S, in accordance with the described structure of multi-pods with Cu core and SR long arms. The elemental distribution in the multipods was further verified using STEM-EDS elemental mapping. Fig. 2h–j illustrates that Cd and S are confined to the arms section, while Cu is only in the center of the structure. Notably, no evidence of cationic exchange was observed either *via* EDX or HRTEM.

The colloidal stability of the various SR-Cu heterojunctions was examined after 15 months of storage (Fig. S3†). The single metal tipped nanorods (SR-e-Cu, SR-s-Cu and SR-c-Cu)



maintained their structural stability, while the highly branched multipods on Cu core demonstrated some tendency to break. This might be related to the formation mechanism, which is based on merging of several individual Cu domains during the synthesis. Note that fragility of tetrapods was previously reported in the literature also for CdTe.<sup>43</sup>

In all cases, we observed that the SR underwent Cu deposition instead of converting to  $\text{Cu}_2\text{Se}@\text{Cu}_2\text{S}$  by cation exchange reaction, and successful formation of the desired heterostructures was achieved. The chemical composition of the as-prepared SR-Cu heterojunctions was further confirmed by X-ray powder diffraction (XRD, Fig. 3a). As expected, the XRD profile of the initial SR is corresponding to the hexagonal wurtzite CdS (JCPDS #00-006-0314) due to the richer abundance of the CdS shell mass with respect to the CdSe core. The SR crystal phase appears to be preserved in all of the SR-Cu heterojunctions. The peaks at  $43.3^\circ$ ,  $50.4^\circ$  and  $74.1^\circ$  in XRD spectra of all the SR-Cu heterojunctions are matched well with the (111), (200) and (220) facets of metallic fcc Cu (JCPDS #04-0836). No additional peaks that belong to  $\text{Cu}_2\text{S}$  were observed, revealing that the cation exchange reaction was prevented. The Cu diffraction peaks of SR-Cu multipods become much stronger and narrower owing to the higher content and larger size of Cu compared to other morphologies, so that the peaks

belonging to SR are not obvious. This XRD pattern zoomed in on Y-axis is given in Fig. S4.† The XRD results further verify the metallic nature of the Cu nanoparticle in the SR-Cu heterojunctions. The average crystallite size of the Cu domains is calculated *via* the Scherrer equation, which is provided in the ESI,† based on the XRD pattern Cu (200). A crystallite size of approximately 13.8 nm and 14.7 nm is calculated for SR-s-Cu, and SR-c-Cu, respectively, in good agreement with the size determined from TEM. For SR-Cu nanomultipods, the crystallite size of 12.9 nm that is calculated by the Scherrer equation is smaller than that of the particles observed in the TEM (Fig. 2b), which further supports the proposed mechanism of merging of individual Cu tips. X-ray photoelectron spectroscopy (XPS) of SR-c-Cu was measured as an example, to investigate the surface chemical state of the metal nanoparticles deposited on SR. As shown in Fig. 3b and c, the characteristic peaks at 405.3 eV (Cd  $3d_{5/2}$ )/412.0 eV (Cd  $3d_{3/2}$ ) in the high-resolution Cd 3d spectrum and 161.5 eV (S  $2p_{3/2}$ )/162.8 eV (S  $2p_{1/2}$ ) in the high-resolution S 2p spectrum are attributed to  $\text{Cd}^{2+}$  and  $\text{S}^{2-}$  of CdS, respectively.<sup>29</sup> In the high-resolution spectrum of Cu 2p (Fig. 3d), the peaks at about 932.2 eV (Cu  $2p_{3/2}$ ) can be assigned to elemental  $\text{Cu}^+$  or  $\text{Cu}^0$  due to the overlapping of their peaks.<sup>44</sup> The weak peak at 933.2 eV could be ascribed to  $\text{Cu}^{2+}$ , which might originate from the CuO and/or  $\text{Cu}(\text{OH})_2$  species because the

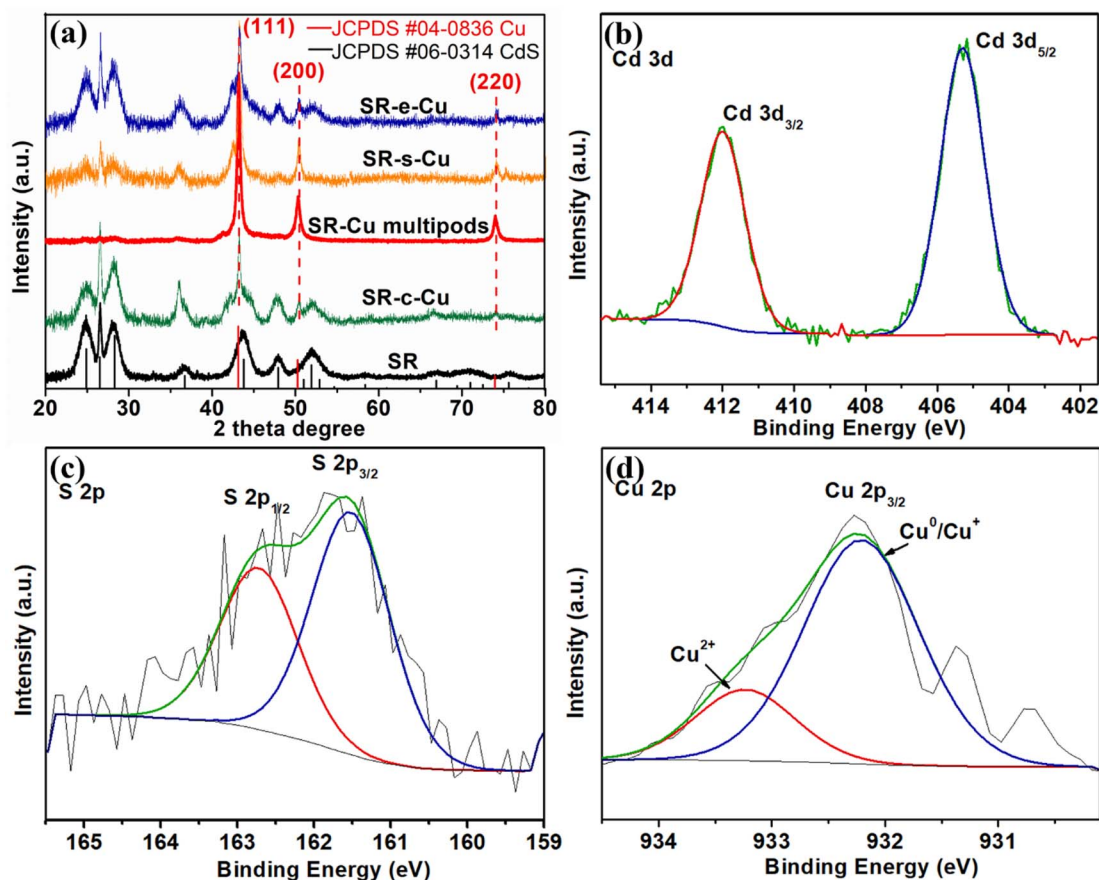


Fig. 3 (a) XRD patterns of SR, SR-c-Cu, SR-e-Cu, SR-s-Cu, and SR-Cu multipods at the range from  $20^\circ$  to  $80^\circ$ . (b–d) High-resolution Cd 3d, S2p and Cu2p XPS spectra of SR-c-Cu, respectively.





sample's surface is inevitably exposed to air when measured.<sup>44</sup> Notably, the XRD results do not show any evidence of the CuO and/or Cu(OH)<sub>2</sub> phase. Hence, we assume that the XPS analysis demonstrates the presence of Cu<sup>2+</sup> ions present only on the surface, or a minor amount of Cu<sub>2</sub>O. In other words, it can be inferred that the Cu on the SR was mainly present in the form of metallic copper.<sup>45</sup>

Control experiments were carried out to explore the role of the TBAB, CuOAc, and TOP used in the synthetic process. Interestingly, when only oleylamine is included as a reducing agent, the TOP<sub>2</sub>-Cu complex cannot be reduced at a temperature of 260 °C. When the reaction temperature was continually increased to 335 °C, free Cu nanocrystals with irregular morphology and wide size distribution were generated, without evidence for heterogenous nucleation on the rod (Fig. S5a†). This observation indicates that the introduction of TBAB is necessary in order to induce reduction of the Cu precursor at reasonable temperature and encourage heterogenous nucleation. Alternative copper(i) salts such as CuBr, CuI and CuCl were examined as a replacement to CuOAc, and the results (Fig. S5b–d†) show all of them are unsuitable for Cu deposition on SR.

In another experiment, triethyl phosphite, a known phosphite that regulates ion exchange reaction kinetics,<sup>46</sup> was applied as substitute for the TOP in the reaction, while CuBr served as the copper(i) precursor. The resulting products (Fig. 4a

and b) are mainly spiral-like nanorods. The EDS spectrum, STEM-EDS elemental mapping, and line-scan analysis (Fig. 4c–i) exhibit evidence for Cd, likely some ion residue in the surrounding the spiral nanorods. Cu and S are clearly seen throughout the rods with homogenous distribution, suggesting a composition of Cu<sub>2</sub>Se@Cu<sub>2</sub>S. The formation of this structure is the result of cation exchange reaction between copper and Cd ion from the SR, which is extracted out of the lattice. Interestingly, the shape of the spiral nanorods is different from the traditional outcome of Cd/Cu cation exchange, which is known to preserve the shape of the rods *via* anionic framework conservation.<sup>47</sup> These findings illustrate that the specific choice of a reducing agent, copper salt and phosphide is quite critical for achieving the deposition of metallic copper on SR, as well as controlling the resultant shape.

Photodeposition of metallic Cu nanocrystals with Cu(NO<sub>3</sub>)<sub>2</sub> as precursor and triethylamine (TEA) as hole scavenger was investigated as a possible alternative route for Cu colloidal reduction deposition pathway (Fig. S6a†). After illumination for 3 h, a small nanoparticle with darker image contrast positioned along the length of nanorods was observed (Fig. S6b–d†), presumably a metallic Cu domain based on the contrast variations. The deposition location on the nanorod's surface might be related to surface defects such as incomplete surface passivation (serving as carrier traps), or simply the location of the CdSe seed.<sup>26</sup> However, STEM-EDX mapping (Fig. S6e–h†)

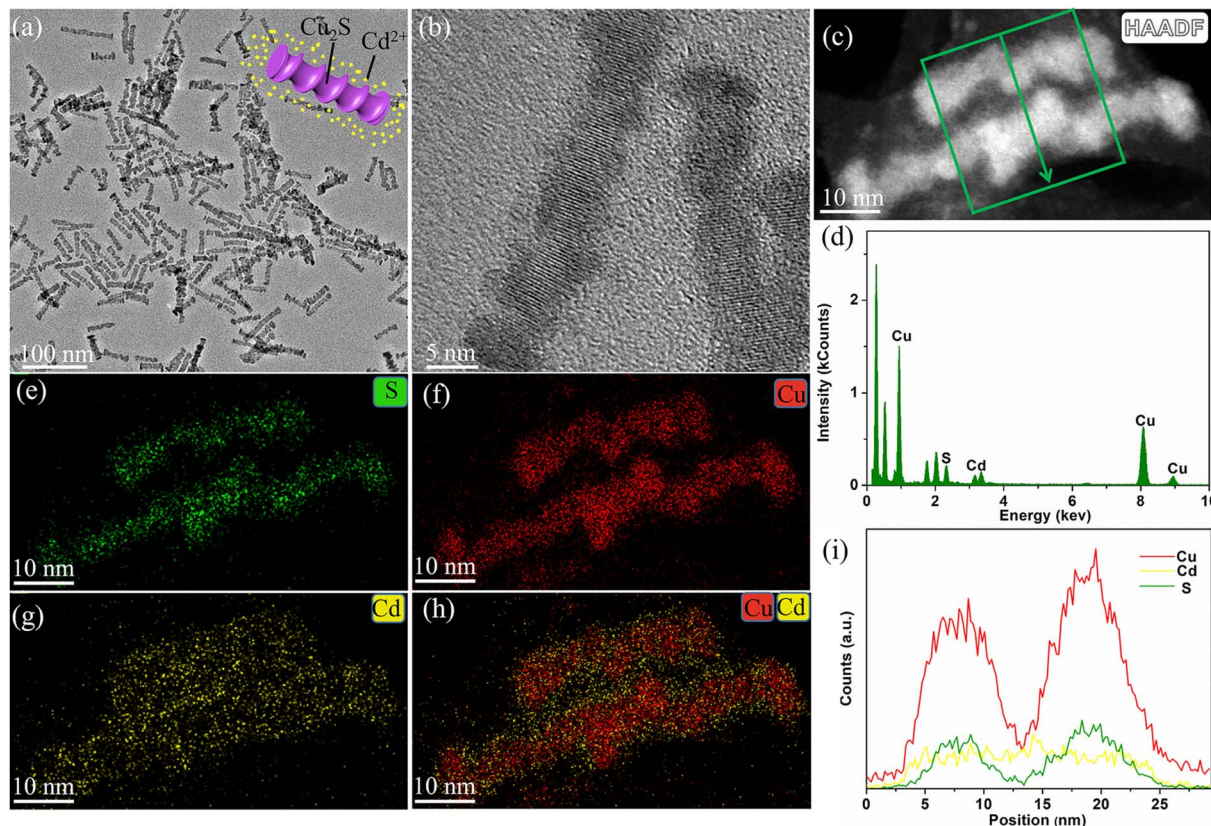


Fig. 4 (a and b) TEM images of spiral nanorods produced by replacing TOP with TBP, and CuAc with CuBr. (c–h) The HAADF image, EDS and its STEM-EDS elemental mapping and (i) EDS line-scan analysis of the rectangular area marked in (c).



confirms that alongside the formation of Cu nanoparticles on the rods, the SR started undergoing conversion to  $(\text{Cu}_2\text{Se}@\text{Cu}_2\text{S})$  due to cation exchange. Notably, this photodeposition strategy provides a new pathway for the synthesis of cadmium-free semiconductor-metal heterojunction, which holds great potential for diverse applications.

## 2.2 Optical properties of the SR-Cu heterojunctions

The optical features of the SR-Cu heterojunctions with different morphologies were evaluated by measuring the UV-visible absorption and PL intensity. The absorption spectrum (Fig. 5a) of the unmodified SR exhibits prominent high-energy peaks below  $\sim 475$  nm ascribed to the absorption from CdS, with additional low intensity contribution at around 575 nm that is ascribed to the CdSe core.<sup>42</sup> The surface plasmon resonance (SPR) absorption of the metallic Cu in the SR-Cu heterojunctions was evident as a broad peak across 525–600 nm that was observed especially for the SR-s-Cu and SR-Cu multipods, with variations that can be attributed to differences in both size and shape, surface state, and the surrounding medium environment of the Cu.<sup>48,49</sup> The SPR bands of Cu for the SR-s-Cu, SR-e-Cu, and SR-Cu multipods are centered at 566, 568, and 576 nm, respectively, while it is not apparent for SR-c-Cu. The SPR band of nanomultipods shows a redshift compared to other samples due to the larger average size of the Cu domains, while the SR-e-Cu and SR-c-Cu have very weak SPR bands, which is related to the smaller sizes of Cu domains.<sup>48</sup> The photoluminescence (PL) spectrum (Fig. 5b) demonstrates that the introduction of a metallic Cu tip results in varying degrees of PL quenching of the SR, likely due to transfer of photoexcited electrons from SR to Cu domains, which is size sensitive and depends on the interplay between the Schottky barrier and Coulomb blockade at the semiconductor-metal interface.<sup>14</sup> The calculated PL quantum yield (PLQY) dropped from  $\sim 73\%$  for bare rods to below 1% for the SR-Cu heterojunctions. The average radiative lifetime obtained by time-resolved PL (TRPL) spectroscopy (Fig. 5c, Table S1†) also decreased from  $\sim 23$  ns to  $\sim 8$ –17 ns when Cu tips were grown on the rods, revealing the activation of some nonradiative decay channels, likely a result of electron transfer from the nanorod to the Cu nanocrystals.<sup>50</sup> These results are in accordance with typical characteristics of semiconductor metal nanoscale hybrids systems, as opposed to reports on plasmon enhanced PL.<sup>51</sup>

## 2.3 Growth mechanism of the SR-Cu heterojunctions

A possible growth mechanism that enables the controllable synthesis of SR-Cu with different morphologies is illustrated in Fig. 7. The most critical aspect in the synthesis process is the introduction of TOP to manipulate the reaction kinetics in order to prevent cation exchange. Different phosphines have been used to control the thermodynamic and kinetic parameters of cation exchange reactions, as was additionally confirmed by our recent work on Ag tipping of SR.<sup>29,46</sup> On the base of the hard and soft (Lewis) acids and bases theory,<sup>52</sup>  $\text{Cu}^+$  cations as soft acid (hardness  $\eta$ , 6.28 eV),<sup>53</sup> tend to combine with soft bases, such as alkyl phosphine (e.g., TOP). In contrast,  $\text{Cd}^{2+}$  as a hard acid ( $\eta$ , 10.29 eV)<sup>53</sup> prefers to ligate with a hard base such as oleylamine, which is beneficial to the extraction of  $\text{Cd}^{2+}$  from the nanocrystals. When TOP as soft base is introduced, the soft acid  $\text{Cu}^+$  cations preferentially combine with the TOP instead of the  $\text{Cd}^{2+}$  cations (hard acid), leaving no driving force to act for Cd extraction. Therefore, prior complexation of  $\text{Cu}^+$  cations with TOP is extremely important to metallic Cu deposition *in lieu* of cation exchange. Without TOP coordination,  $\text{Cu}^+$  cations prefer to replace  $\text{Cd}^{2+}$  in the nanocrystals, and in some cases, it might even destroy the original rod-like, due to abrupt changes or requirements for structure reconstruction (Fig. S7†). These reflect some of the synthetic challenges in the field.<sup>39,54</sup>

The complexation of  $\text{Cu}^+$  cations with TOP was determined *via* electrospray ionization mass spectrometry (ESI-MS) and nuclear magnetic resonance (NMR) spectroscopy analysis of the complex that is obtained from dissolving CuOAc in TOP. The ESI mass spectrum of TOP-Cu complex (Fig. 6a) exhibits a prominent peak at  $m/z$  803 (100%) of formula  $[\text{TOP}_2\text{Cu}]^+$ , which is in agreement with the calculated isotopic mass distributions for  $[\text{C}_{48}\text{H}_{102}\text{P}_2\text{Cu}]^+$  (Fig. S8a†). The molecular structure of  $\text{TOP}_2\text{-Cu}$  complex is expected to display a linear coordination geometry whereby the copper atom is coordinated to only two phosphines, resembling well-established linear copper(i) complexes such as  $[\text{Cu}(\text{PBz}_3)_2]\text{PF}_6$ .<sup>55</sup> The coordination environment of copper(i) with TOP was examined by  $^{31}\text{P}$   $\{^1\text{H}\}$  NMR spectra (Fig. 6b), where a downfield shift and broadening of the  $^{31}\text{P}$  resonance for all the synthesized  $\text{TOP}_2\text{-Cu}$  complexes compared with the pure TOP were observed. The downfield shift is attributed to deshielding effect, as the electron density around phosphorus decreases upon coordination of the TOP to

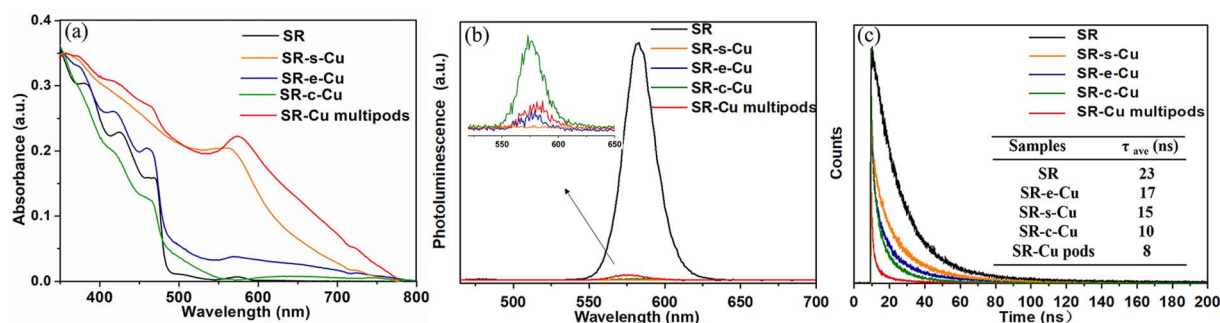


Fig. 5 (a–c) The UV-vis absorption, PL spectra and normalized TRPL decay spectra of the samples.



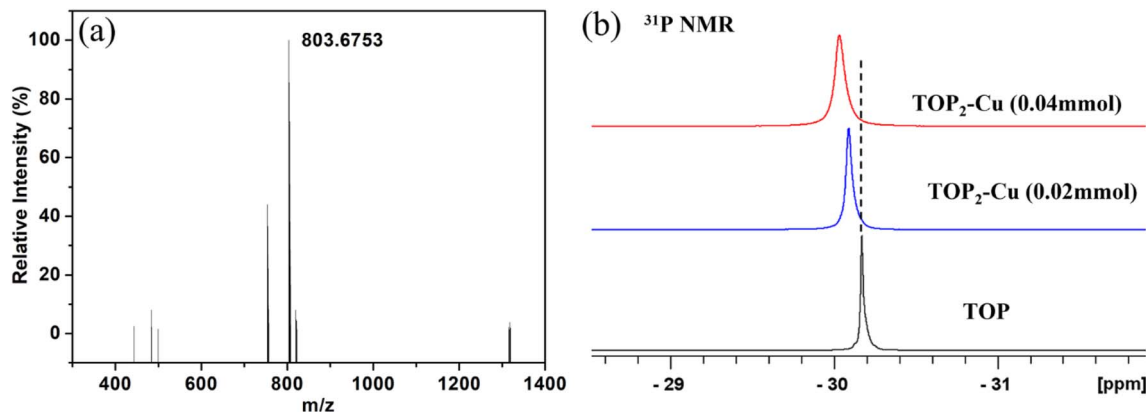


Fig. 6 (a) ESI-MS for the TOP<sub>2</sub>-Cu complex, (b) <sup>31</sup>P {<sup>1</sup>H} NMR spectra of TOP and TOP<sub>2</sub>-Cu complexes synthesized by adding 0.02 mmol or 0.04 mmol of CuOAc.

copper ion, resulting from the donation of electrons from P to Cu<sup>+</sup>. A more pronounced downfield shift was induced by coordinating higher amount of Cu to TOP (Fig. S8b†) to form TOP<sub>2</sub>-Cu complex with higher concentration. Once the coordination between TOP and Cu ion is established, the complex was further reduced, leading to the growth of metallic Cu on SR.

In the presence of a strong reducing agent, such as TBAB/oleylamine, the coordination between Cu<sup>+</sup> cations and TOP is weakened and Cu<sup>+</sup> can be reduced to the metallic state. As demonstrated in the course of this work, precise control over the shape of the nanocrystals can be achieved by adjusting reaction parameters such as temperature, reducing agent, and precursor concentration. According to the chosen synthetic conditions, reactions will be conducted under thermodynamic or kinetic regimes, giving access to nanocrystals with different configurations.<sup>56–60</sup> Specifically, the nanocrystals will assume different shapes based on the global minimum in Gibbs free energy or local minima, as directed by either thermodynamically or kinetically driven pathways. The preferred pathway may be encouraged by varying the temperature and monomer flux.<sup>58</sup> Notably, high temperature and low monomer flux benefit the thermodynamic regime, while the opposite situation will favor the kinetic regime.<sup>58</sup>

FCC Cu metal, with a specific surface energies for the low-index crystallographic facets that follow the order:  $\gamma(111) <$

$\gamma(100) < \gamma(110)$ , are expected to be thermodynamically stable as an octahedron, where the (111) facets are all exposed on the surface.<sup>61</sup> Considering the minimization of the total surface free energy, however, a cube shape has a smaller surface area-to-volume ratio in comparison with an octahedron of the same volume, which is expected to result in a truncated octahedron enclosed by the (111) and (100) facets. This shape may be regarded as a quasi-sphere for smaller size particles.<sup>62</sup> In view of the above analysis the Cu nanocrystals with alternative shapes (*i.e.*, cubes, tetrahedra, *etc.*) might be the result of a kinetically driven reaction.

In our system, the Cu(0) from the reduction of the complex can be regarded as the monomeric species, and the intermediates (*i.e.*, Cu(I)) conversion kinetics into Cu(0) are representative of the monomer flux.<sup>63</sup> The TBAB/oleylamine as the strong reducing agents prefer to produce the nanocrystals with equilibrium shapes.<sup>64</sup> The injection of the preformed TBAB/oleylamine reducing agent into the mixture of SR and TOP<sub>2</sub>-Cu complex at 260 °C induces an immediate color change to dark purple, presumably due to Cu(0) nucleation. This is followed by the formation of spherical Cu nanocrystal on SR under thermodynamic control, both with a high CuOAc concentration (0.04 mmol) and with a low CuOAc concentration (0.02 mmol). It is presumed that when the reducing agent is injected at this high temperature, the final configuration of Cu nanocrystal is

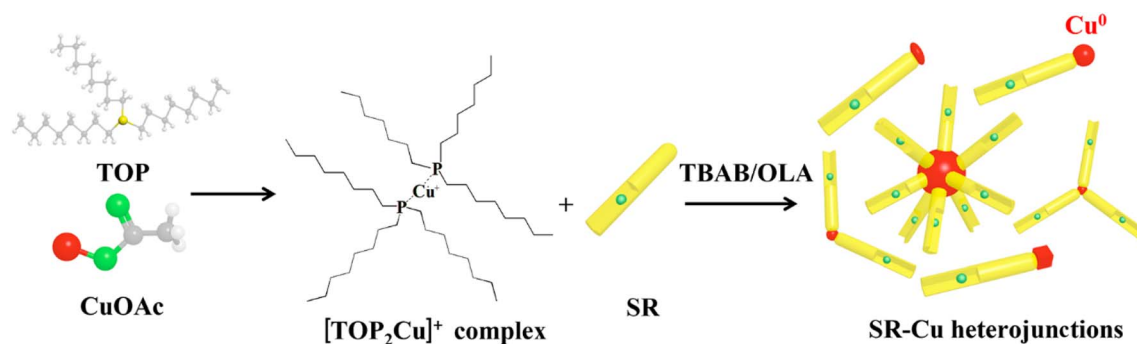


Fig. 7 Illustration of possible growth mechanism for the formation of SR-Cu heterojunctions.



dependent on the correlative thermodynamic barriers rather than precursor concentrations. When the injection temperature is decreased to room temperature, a gradual flux of Cu(0) monomers is produced during the heating ramp from room temperature until the 260 °C; thus, the reaction is under kinetic control and elliptic or cubic Cu domains are grown on the SR as the ultimate product.

The formation of a SR-Cu heterojunction is energetically favorable. The observed selective growth regime of the Cu domain on the basal ends of the SR is expected in light of previous SR-metal hybrids that displayed similar morphology. However, the dominance of mono tip formation in this case is unique and might be explained by the joint effect of interfacial strain between lattices and the shape anisotropy of the rods. The metal preferentially deposits onto the SR apexes due to their higher chemical reactivity/surface energy in comparison to the rod's sidewalls. The S-rich end of the SR is considered the side that favors the growth of metals in general due to the driving force from the electrostatic attraction and weaker ligand coverage,<sup>65</sup> and this might be more significant in the specific case of Cu.

### 3. Conclusion

In summary, SR-Cu heterojunctions with interesting morphologies, including elliptic, spherical, and cubic Cu tips that are grown on at one end of the nanorods, as well as a central Cu domain with SR branches (nanomultipods) have been successfully produced. The synthetic procedure follows heterogeneous nucleation and growth of metallic Cu on SR substrates. Independently tunable SR-Cu heterojunctions of different configurations and sizes are obtained by adjustment of selected key reaction parameters, which enable manipulation between kinetically and thermodynamically governed reaction pathways. The mechanism, which enables mitigation of cation exchange and precise control over shape, is discussed. The novel SR-Cu heterojunctions that are developed in the course of this work may be beneficial for a wide range of applications. Specifically, for photocatalysis they are expected to facilitate the anticipated shape-functionality studies in nanoscale hybrid systems, with potential influence on activity, selectivity, and stability.

## 4. Experimental section

### 4.1 Synthesis of SR-Cu hetero-nanostructures

SR-e-Cu were prepared by decomposition of copper(i) acetate (CuOAc). In a typical synthesis, 0.02 mmol copper(i) acetate (CuOAc) was dissolved in 2 mL of trioctylphosphine (TOP) under Ar at 150 °C (TOP<sub>2</sub>-Cu complex). A volume of 400 µL of CdSe@CdS nanorods in toluene (Cd<sup>2+</sup> concentration ~ 7 mM) was precipitated with methanol and then dispersed into 1 mL TOP containing 2 mmol borane-*tert*-butylamine complex (TBAB). After that, the nanorods solution was injected into the TOP<sub>2</sub>-Cu complex at room temperature. The mixture was heated at 260 °C for 30 min. After the reaction, the sample was purified with toluene, ethanol, and methanol several times and

was finally dispersed in toluene for further characterization. For the preparation of SR-s-Cu, similarly 0.04 mmol CuOAc was used but TBAB dissolved in 1 mL of oleylamine (OLA) by sonication was injected into the mixture of TOP<sub>2</sub>-Cu complex and CdSe@CdS nanorods/ToP solution at 260 °C and kept for 30 min. For the synthesis of SR-Cu nanomultipods, same as the synthesis of the SR-s-Cu, but 0.02 mmol CuOAc was used as the precursor. For the synthesis of SR-c-Cu, similar to the SR-Cu nanomultipods case but the TBAB/OLA reducing agent was injected at room temperature.

### 4.2 Characterizations

Transmission electron microscopy (TEM) was performed by Tecnai G<sup>2</sup> T20 S-Twin TEM under 200 keV. High-angle annular dark-field (HAADF) scanning TEM-energy-dispersive X-ray spectroscopy (HAADF-STEM-EDX) maps was collected by an FEI Titan Cubed Themis G<sup>2</sup> 60–300 microscope at an accelerating voltage of 200 keV. X-ray powder diffraction (XRD) spectrum was obtained by using Rigaku SmartLab X-ray diffractometer using Cu K $\alpha$  radiation. Photoluminescence (PL) spectrum was measured by a Fluorolog-3 Fluorometer at room temperature, under 455 nm excitation wavelength and UV-vis absorption spectroscopy was executed with an Agilent Cary 5000 UV-vis-NIR spectrophotometer. Nuclear Magnetic Resonance (NMR): <sup>31</sup>P{<sup>1</sup>H} spectra were recorded on a 300 MHz Bruker Advance spectrometer with CDCl<sub>3</sub> as the deuterated solvent. Different amount of Cu (0.02 mmol, 0.04 mmol, 0.4 mmol and 1 mmol) was dissolved into 2 mL of TOP at 150 °C to prepare TOP<sub>2</sub>-Cu stock solution. The TOP or TOP<sub>2</sub>-Cu stock solution (0.5 mL) was diluted with 0.5 mL of CDCl<sub>3</sub>. An external standard H<sub>3</sub>PO<sub>4</sub> (85%) was used for calibrating the <sup>31</sup>P NMR spectrum. Electrospray ionization-mass spectrometry (ESI-MS) measurements were performed on a maxis Impact mass spectrometer (Bruker). TOP or TOP<sub>2</sub>-Cu (0.04 mmol) stock solution (0.8 mL) was diluted with 1 mL of chloroform.

### Data availability

The data supporting this article have been uploaded as part of the ESI.†

### Author contributions

Y. C. conducted the investigation under L. A.'s supervision. Y. C. and L. A. wrote the manuscript.

### Conflicts of interest

The authors declare no conflict of interest.

### Acknowledgements

We gratefully acknowledge support from the Israel Science Foundation Center of Excellence (grant #2171/17). This work was performed in the framework of the Russell Berrie Nanotechnology Institute (RBNI) and the Nancy and Stephen Grand



Technion Energy Program (GTEP). We appreciate the help of Dr Kamira Weineld-Cohen for XPS measurement.

## References

- 1 L. Amirav and A. P. Alivisatos, Photocatalytic hydrogen production with tunable nanorod heterostructures, *J. Phys. Chem. Lett.*, 2010, **1**(7), 1051–1054.
- 2 P. Kalisman, Y. Nakibli and L. Amirav, Perfect photon-to-hydrogen conversion efficiency, *Nano Lett.*, 2016, **16**(3), 1776–1781.
- 3 A. Agosti, Y. Nakibli, L. Amirav and G. Bergamini, Photosynthetic H<sub>2</sub> generation and organic transformations with CdSe@CdS-Pt nanorods for highly efficient solar-to-chemical energy conversion, *Nano Energy*, 2020, **70**, 104510.
- 4 T. Rosner, N. G. Pavlopoulos, H. Shoyhet, M. Micheel, M. Wächter, N. Adir and L. Amirav, The Other Dimension—Tuning Hole Extraction via Nanorod Width, *Nanomaterials*, 2022, **12**(19), 3343.
- 5 K. Wu and T. Lian, Quantum confined colloidal nanorod heterostructures for solar-to-fuel conversion, *Chem. Soc. Rev.*, 2016, **45**(14), 3781–3810.
- 6 A. Sitt, F. D. Sala, G. Menagen and U. Banin, Multiexciton engineering in seeded core/shell nanorods: transfer from type-I to quasi-type-II regimes, *Nano Lett.*, 2009, **9**(10), 3470–3476.
- 7 K. Dong, C. Pezzetta, Q. C. Chen, A. Kaushansky, A. Agosti, G. Bergamini, R. Davidson and L. Amirav, Nanorod Photocatalysts for C–O Cross-Coupling Reactions, *ChemCatChem*, 2022, **14**(15), e202200477.
- 8 A. A. Pawar, S. Halivni, N. Waiskopf, Y. Ben-Shahar, M. Soreni-Harari, S. Bergbreiter, U. Banin and S. Magdassi, Rapid three-dimensional printing in water using semiconductor-metal hybrid nanoparticles as photoinitiators, *Nano Lett.*, 2017, **17**(7), 4497–4501.
- 9 M. T. Sheldon, P.-E. Trudeau, T. Mokari, L.-W. Wang and A. P. Alivisatos, Enhanced semiconductor nanocrystal conductance via solution grown contacts, *Nano Lett.*, 2009, **9**(11), 3676–3682.
- 10 H. Steinberg, O. Wolf, A. Faust, A. Salant, Y. Lilach, O. Millo and U. Banin, Electrical current switching in single CdSe nanorods, *Nano Lett.*, 2010, **10**(7), 2416–2420.
- 11 C. R. Kagan, E. Lifshitz, E. H. Sargent and D. V. Talapin, Building devices from colloidal quantum dots, *Science*, 2016, **353**(6302), aac5523.
- 12 Y. Nakibli, P. Kalisman and L. Amirav, Less is more: The case of metal cocatalysts, *J. Phys. Chem. Lett.*, 2015, **6**(12), 2265–2268.
- 13 T. Simon, M. T. Carlson, J. K. Stolarczyk and J. Feldmann, Electron transfer rate vs recombination losses in photocatalytic H<sub>2</sub> generation on Pt-decorated CdS nanorods, *ACS Energy Lett.*, 2016, **1**(6), 1137–1142.
- 14 Y. Nakibli, Y. Mazal, Y. Dubi, M. Wächter and L. Amirav, Size matters: Cocatalyst size effect on charge transfer and photocatalytic activity, *Nano Lett.*, 2018, **18**(1), 357–364.
- 15 Y. Ben-Shahar, F. Scotognella, I. Kriegel, L. Moretti, G. Cerullo, E. Rabani and U. Banin, Optimal metal domain size for photocatalysis with hybrid semiconductor-metal nanorods, *Nat. Commun.*, 2016, **7**(1), 1–7.
- 16 Y. Liu, W. Yang, Q. Chen, D. A. Cullen, Z. Xie and T. Lian, Pt Particle Size Affects Both the Charge Separation and Water Reduction Efficiencies of CdS-Pt Nanorod Photocatalysts for Light Driven H<sub>2</sub> Generation, *J. Am. Chem. Soc.*, 2022, **144**(6), 2705–2715.
- 17 F. F. Schweinberger, M. J. Berr, M. Döblinger, C. Wolff, K. E. Sanwald, A. S. Crampton, C. J. Ridge, F. Jackel, J. Feldmann and M. Tschurl, Cluster size effects in the photocatalytic hydrogen evolution reaction, *J. Am. Chem. Soc.*, 2013, **135**(36), 13262–13265.
- 18 L. Amirav and M. Wächter, Nano Schottky?, *Nano Lett.*, 2022, **22**(24), 9783–9785.
- 19 M. Luo, W. Yao, C. Huang, Q. Wu and Q. Xu, Shape effects of Pt nanoparticles on hydrogen production via Pt/CdS photocatalysts under visible light, *J. Mater. Chem. A*, 2015, **3**(26), 13884–13891.
- 20 P. Mäki-Arvela and D. Y. Murzin, Effect of metal particle shape on hydrogen assisted reactions, *Appl. Catal., A*, 2021, **618**, 118140.
- 21 S. Cao, F. F. Tao, Y. Tang, Y. Li and J. Yu, Size-and shape-dependent catalytic performances of oxidation and reduction reactions on nanocatalysts, *Chem. Soc. Rev.*, 2016, **45**(17), 4747–4765.
- 22 L. Liu and A. Corma, Metal catalysts for heterogeneous catalysis: from single atoms to nanoclusters and nanoparticles, *Chem. Rev.*, 2018, **118**(10), 4981–5079.
- 23 G. A. Somorjai and J. Carrazza, Structure sensitivity of catalytic reactions, *Ind. Eng. Chem. Fundam.*, 1986, **25**(1), 63–69.
- 24 G. Menagen, J. E. Macdonald, Y. Shemesh, I. Popov and U. Banin, Au growth on semiconductor nanorods: photoinduced versus thermal growth mechanisms, *J. Am. Chem. Soc.*, 2009, **131**(47), 17406–17411.
- 25 S. E. Habas, P. Yang and T. Mokari, Selective growth of metal and binary metal tips on CdS nanorods, *J. Am. Chem. Soc.*, 2008, **130**(11), 3294–3295.
- 26 G. Dukovic, M. G. Merkle, J. H. Nelson, S. M. Hughes and A. P. Alivisatos, Photodeposition of Pt on colloidal CdS and CdSe/CdS semiconductor nanostructures, *Adv. Mater.*, 2008, **20**(22), 4306–4311.
- 27 E. Aronovitch, P. Kalisman, L. Houben, L. Amirav and M. Bar-Sadan, Stability of seeded rod photocatalysts: atomic scale view, *Chem. Mater.*, 2016, **28**(5), 1546–1552.
- 28 S. Deka, A. Falqui, G. Bertonni, C. Sangregorio, G. Poneti, G. Morello, M. D. Giorgi, C. Giannini, R. Cingolani and L. Manna, Fluorescent asymmetrically cobalt-tipped CdSe@CdS core@shell nanorod heterostructures exhibiting room-temperature ferromagnetic behavior, *J. Am. Chem. Soc.*, 2009, **131**(35), 12817–12828.
- 29 K. Dong, Q.-C. Chen, Z. Xing, Y. Chen, Y. Qi, N. G. Pavlopoulos and L. Amirav, Silver Tipping of CdSe@CdS Nanorods: How To Avoid Cation Exchange, *Chem. Mater.*, 2021, **33**(16), 6394–6402.



- 30 Y. Nakibli and L. Amirav, Selective growth of Ni tips on nanorod photocatalysts, *Chem. Mater.*, 2016, **28**(13), 4524–4527.
- 31 E. Aronovitch, P. Kalisman, S. Mangel, L. Houben, L. Amirav and M. Bar-Sadan, Designing bimetallic co-catalysts: a party of two, *J. Phys. Chem. Lett.*, 2015, **6**(18), 3760–3764.
- 32 P. Kalisman, L. Houben, E. Aronovitch, Y. Kauffmann, M. Bar-Sadan and L. Amirav, The golden gate to photocatalytic hydrogen production, *J. Mater. Chem. A*, 2015, **3**(39), 19679–19682.
- 33 D. L. Edelstein, *Mineral commodity summaries: copper*, US Geological Survey, 2011.
- 34 A. Loiudice, P. Lobaccaro, E. A. Kamali, T. Thao, B. H. Huang, J. W. Ager and R. Buonsanti, Tailoring copper nanocrystals towards C2 products in electrochemical CO2 reduction, *Angew. Chem., Int. Ed.*, 2016, **55**(19), 5789–5792.
- 35 M. B. Gawande, A. Goswami, F.-X. Felpin, T. Asefa, X. Huang, R. Silva, X. Zou, R. Zboril and R. S. Varma, Cu and Cu-based nanoparticles: synthesis and applications in catalysis, *Chem. Rev.*, 2016, **116**(6), 3722–3811.
- 36 H. Wu, L. Hu, M. W. Rowell, D. Kong, J. J. Cha, J. R. McDonough, J. Zhu, Y. Yang, M. D. McGehee and Y. Cui, Electrospun metal nanofiber webs as high-performance transparent electrode, *Nano Lett.*, 2010, **10**(10), 4242–4248.
- 37 A. R. Rathmell and B. J. Wiley, The synthesis and coating of long, thin copper nanowires to make flexible, transparent conducting films on plastic substrates, *Adv. Mater.*, 2011, **23**(41), 4798–4803.
- 38 Q. Shao, R. Que, M. Shao, L. Cheng and S. T. Lee, Copper nanoparticles grafted on a silicon wafer and their excellent surface-enhanced Raman scattering, *Adv. Funct. Mater.*, 2012, **22**(10), 2067–2070.
- 39 D. H. Son, S. M. Hughes, Y. Yin and A. P. Alivisatos, Cation exchange reactions in ionic nanocrystals, *Science*, 2004, **306**(5698), 1009–1012.
- 40 H. Guo, Y. Chen, H. Ping, J. Jin and D.-L. Peng, Facile synthesis of Cu and Cu@Cu–Ni nanocubes and nanowires in hydrophobic solution in the presence of nickel and chloride ions, *Nanoscale*, 2013, **5**(6), 2394–2402.
- 41 M. Strach, V. Mantella, J. R. Pankhurst, P. Iyengar, A. Loiudice, S. Das, C. m. Corminboeuf, W. van Beek and R. Buonsanti, Insights into Reaction Intermediates to Predict Synthetic Pathways for Shape-Controlled Metal Nanocrystals, *J. Am. Chem. Soc.*, 2019, **141**(41), 16312–16322.
- 42 L. Carbone, C. Nobile, M. De Giorgi, F. D. Sala, G. Morello, P. Pompa, M. Hytch, E. Snoeck, A. Fiore, I. R. Franchini, M. Nadasan, A. F. Silvestre, L. Chiodo, S. Kudera, R. Cingolani, R. Krahne and L. Manna, Synthesis and Micrometer-Scale Assembly of Colloidal CdSe/CdS Nanorods Prepared by a Seeded Growth Approach, *Nano Lett.*, 2007, **7**(10), 2942–2950.
- 43 L. Fang, J. Y. Park, Y. Cui, P. Alivisatos, J. Shcrier, B. Lee, L.-W. Wang and M. Salmeron, Mechanical and electrical properties of CdTe tetrapods studied by atomic force microscopy, *J. Chem. Phys.*, 2007, **127**(18), 184704.
- 44 Y. Wang, Q. Zhang, Y. Wang, L. V. Besteiro, Y. Liu, H. Tan, Z. M. Wang, A. O. Govorov, J. Z. Zhang and J. K. Cooper, Ultrastable Plasmonic Cu-Based Core–Shell Nanoparticles, *Chem. Mater.*, 2020, **33**(2), 695–705.
- 45 L. Rout, A. Kumar, R. S. Dhaka and P. Dash, Bimetallic Ag–Cu alloy nanoparticles as a highly active catalyst for the enamination of 1, 3-dicarbonyl compounds, *RSC Adv.*, 2016, **6**(55), 49923–49940.
- 46 J. Gui, M. Ji, J. Liu, M. Xu, J. Zhang and H. Zhu, Phosphine-Initiated Cation Exchange for Precisely Tailoring Composition and Properties of Semiconductor Nanostructures: Old Concept, New Applications, *Angew. Chem.*, 2015, **127**(12), 3754–3758.
- 47 P. K. Jain, L. Amirav, S. Aloni and A. P. Alivisatos, Nanoheterostructure cation exchange: anionic framework conservation, *J. Am. Chem. Soc.*, 2010, **132**(29), 9997–9999.
- 48 D. Zeng, P. Gong, Y. Chen, Q. Zhang, Q. Xie and D.-L. Peng, Colloidal synthesis of Cu–ZnO and Cu@ CuNi–ZnO hybrid nanocrystals with controlled morphologies and multifunctional properties, *Nanoscale*, 2016, **8**(22), 11602–11610.
- 49 Y. Zhang, P. Zhu, G. Li, W. Wang, L. Chen, D. D. Lu, R. Sun, F. Zhou and C. Wong, Highly stable and re-dispersible nano Cu hydrosols with sensitively size-dependent catalytic and antibacterial activities, *Nanoscale*, 2015, **7**(32), 13775–13783.
- 50 K. Hosoki, T. Tayagaki, S. Yamamoto, K. Matsuda and Y. Kanemitsu, Direct and stepwise energy transfer from excitons to plasmons in close-packed metal and semiconductor nanoparticle monolayer films, *Phys. Rev. Lett.*, 2008, **100**(20), 207404.
- 51 R. Jiang, B. Li, C. Fang and J. Wang, Metal/semiconductor hybrid nanostructures for plasmon-enhanced applications, *Adv. Mater.*, 2014, **26**(31), 5274–5309.
- 52 L. De Trizio and L. Manna, Forging colloidal nanostructures via cation exchange reactions, *Chem. Rev.*, 2016, **116**(18), 10852–10887.
- 53 R. G. Pearson, Absolute electronegativity and hardness: application to inorganic chemistry, *Inorg. Chem.*, 1988, **27**(4), 734–740.
- 54 X. Cheng, J. Liu, X. Wan, H. Wang, Y. Li, J. Liu, H. Rong, M. Xu, W. Chen and J. Zhang, Phosphine ligand-mediated kinetics manipulation of aqueous cation exchange: a case study on the synthesis of Au@SnS<sub>x</sub> core–shell nanocrystals for photoelectrochemical water splitting, *Chem. Commun.*, 2018, **54**(71), 9993–9996.
- 55 E. W. Ainscough, A. M. Brodie, A. K. Burrell, J. V. Hanna, P. C. Healy and J. M. Waters, Two-Coordinate Tribenzylphosphine (PBz3) Complexes of Copper(I): Solid State 31P NMR Studies and the Crystal Structure of [Cu(PBz3)2]PF6, *Inorg. Chem.*, 1999, **38**(1), 201–203.
- 56 F. Wang, V. N. Richards, S. P. Shields and W. E. Buhro, Kinetics and mechanisms of aggregative nanocrystal growth, *Chem. Mater.*, 2014, **26**(1), 5–21.
- 57 D. Gebauer and S. E. Wolf, Designing solid materials from their solute state: a shift in paradigms toward a holistic approach in functional materials chemistry, *J. Am. Chem. Soc.*, 2019, **141**(11), 4490–4504.





- 58 Y. Xia, X. Xia and H.-C. Peng, Shape-controlled synthesis of colloidal metal nanocrystals: thermodynamic versus kinetic products, *J. Am. Chem. Soc.*, 2015, **137**(25), 7947–7966.
- 59 J. Lee, J. Yang, S. G. Kwon and T. Hyeon, Nonclassical nucleation and growth of inorganic nanoparticles, *Nat. Rev. Mater.*, 2016, **1**(8), 1–16.
- 60 Y. Xia, Y. Xiong, B. Lim and S. E. Skrabalak, Shape-controlled synthesis of metal nanocrystals: simple chemistry meets complex physics?, *Angew. Chem., Int. Ed.*, 2009, **48**(1), 60–103.
- 61 Z. L. Wang, Transmission Electron Microscopy of Shape-Controlled Nanocrystals and Their Assemblies, *J. Phys. Chem. B*, 2000, **104**(6), 1153–1175.
- 62 J. Yang, M. K. Choi, D. H. Kim and T. Hyeon, Designed assembly and integration of colloidal nanocrystals for device applications, *Adv. Mater.*, 2016, **28**(6), 1176–1207.
- 63 S. Nishimura, A. Takagaki, S. Maenosono and K. Ebitani, In situ time-resolved XAFS study on the formation mechanism of Cu nanoparticles using poly (N-vinyl-2-pyrrolidone) as a capping agent, *Langmuir*, 2010, **26**(6), 4473–4479.
- 64 T. Yao, S. Liu, Z. Sun, Y. Li, S. He, H. Cheng, Y. Xie, Q. Liu, Y. Jiang and Z. Wu, Probing nucleation pathways for morphological manipulation of platinum nanocrystals, *J. Am. Chem. Soc.*, 2012, **134**(22), 9410–9416.
- 65 Z. A. Peng and X. Peng, Mechanisms of the shape evolution of CdSe nanocrystals, *J. Am. Chem. Soc.*, 2001, **123**(7), 1389–1395.

